

Silicon and germanium adamantane and diamantane monolayers as two-dimensional anisotropic direct-gap semiconductors

G. Santos-Castro¹,¹ T. Pandey,² C. H. Vito Bruno,¹ E. W. Santos Caetano,^{3,4}
M. V. Milošević,^{2,5,6,*} A. Chaves^{1,2,†} and V. N. Freire¹

¹*Departamento de Física, Universidade Federal do Ceará, Caixa Postal 6030, 60455-760 Fortaleza, Ceará, Brazil*

²*Department of Physics, University of Antwerp, Groenenborgerlaan 171, B-2020 Antwerp, Belgium*

³*Programa de Pós-Graduação em Engenharia de Telecomunicações (PPGET), Instituto Federal de Educação, Ciência e Tecnologia do Ceará, Campus Fortaleza, 60040-531, Fortaleza, CE, Brazil*

⁴*Departamento de Física e Matemática, Instituto Federal de Educação,*

Ciência e Tecnologia do Ceará, Campus Fortaleza, 60040-531, Fortaleza, CE, Brazil

⁵*NANOLab Center of Excellence, University of Antwerp, Antwerp, Belgium*

⁶*Instituto de Física, Universidade Federal de Mato Grosso, 78060-900 Cuiabá, Mato Grosso, Brazil*



(Received 8 December 2022; revised 28 April 2023; accepted 13 June 2023; published 5 July 2023)

Structural and electronic properties of silicon and germanium monolayers with two different diamondoid crystal structures are detailed *ab initio*. Our results show that, despite Si and Ge being well-known indirect gap semiconductors in their bulk form, their adamantane and diamantane monolayers can exhibit optically active direct gap in the visible frequency range, with highly anisotropic effective masses, depending on the monolayer crystal structure. Moreover, we reveal that gaps in these materials are highly tunable with applied strain. These stable monolayer forms of Si and Ge are therefore expected to help bridging the gap between the fast growing area of opto-electronics in two-dimensional materials and the established silicon-based technologies.

DOI: [10.1103/PhysRevB.108.035302](https://doi.org/10.1103/PhysRevB.108.035302)

I. INTRODUCTION

Silicon is the basic element of modern (micro) electronics [1,2]. Due to its excellent electronic mobility, in addition to its high abundance in the Earth's crust and its nontoxicity, it is of fundamental importance for manufacturing semiconductors and photovoltaic materials [2–4]. Crystalline silicon is a semiconductor with an indirect band gap, transmitting more than 95% of all wavelengths of infrared spectrum [3], while silicon nanostructures can present direct band gap and emit visible-spectrum electromagnetic radiation [1,5,6] or even be a good conductor [7]. Germanium is also an elementary semiconductor of major importance in the field of electronics [3,8]. Crystalline germanium doped with arsenic, gallium, or other elements is used as transistor component in a number of electronic applications [8,9]. Germanium nanostructures present physical properties of relevance to new technologies [5,10], such as applications in infrared optoelectronics [10]. The unique allotropic affinity of nanostructures compared to the bulk material points to their more versatile integration strategies and benefits for semiconductor technology and other applications [4,11,12].

Borlido *et al.* [13] predicted the existence of two-dimensional (2D) stable silicon crystal structures, based on reconstructed silicene on Ag (1 1 1) substrate, such as zigzag and armchair dumbbell silicene nanosheets, which are both

indirect gap semiconductors (with gaps of 1.11 eV and 1.60 eV, respectively), as obtained by first-principles calculations using the Heyd-Scuseria-Ernzerhof (HSE06) functional [13]. Hydrogen functionalization of these structures is energetically favorable and hydrogenated zigzag and armchair dumbbell silicene nanosheets were shown to be semiconductors like their pristine counterparts, but with larger band gaps (2.07 eV and 1.78 eV, respectively), with electronic band features sensitive to strains [14]. In addition, they also confirmed by theoretical studies that the hydrogenated structure has robust structural stabilities, which are essential for their practical potential applications [14]. Other 2D allotropic silicon structures have been investigated, such as silicene, that presents an extremely low thermoelectric performance, but hydrogenation can be an effective band regulation strategy in this case, considering the hydrogenation ratio with the method of changing the geometric structure, that would modify the band structure to obtain an ideal band gap value and thermoelectric performance [15]. In experimental terms, the dumbbell silicene phase was experimentally realized by controlled growth of Si pentamer chains on Ag(110) substrate [16]. Half-hydrogenated structures of silicene and germanene (2D allotropic phase of Germanium) have already been synthesized, where one Si (or Ge) sublattice is fully H saturated and the other sublattice is intact. These structures showed stability and a large bandgap compared to their pure counterparts [17,18].

The crystal lattice of bulk silicon and germanium is the same as in diamond. Another material family that presents a structure similar to the rigid structure of diamond are

*milorad.milosevic@uantwerpen.be

†andrey@fisica.ufc.br

diamondoids, the hydrocarbon molecules $C_{4n+6}H_{4n+12}$, where n refers to the quantity and arrangement of “cages” that form the unit cell [19,20]. The simplest polycyclic diamond is the equivalent of $n = 1$ diamondoid $C_{10}H_{16}$, and these are called adamantanes [21]. Sila- and germa-adamantane ($Si_{10}H_{16}$ and $Ge_{10}H_{16}$) have the same structural form as hydrocarbon adamantane, however, their electronic properties are less affected by hydrogen termination [22]. Monolayers can be constructed from isolated sila- or germa-adamantane molecules, considering two possible configurations for the connection among unit cells, allowing one to form monolayers composed of one or two “cages” of silicon or germanium, hydrogenated on the surface. In an equivalent perspective, these structures can also be visualized as isolated planes in the (1 0 0) and (1 1 1) directions of the diamond bulk structure, passivated with hydrogen, whose unitary part corresponds to a single and two “cages,” respectively. We name the resulting (Planar ADAmantane) structures respectively PADA-I and PADA-II, where I and II represents the number/arrangement of “cages” that form the diamond base unit of the planar monolayer.

In this paper, we theoretically detail the mechanical and (piezo-)electronic properties of Si and Ge adamantane and diamantane monolayers, i.e., the PADA-I and PADA-II planes in our nomenclature. We employ *ab initio* density functional theory (DFT) methods using the hybrid functionals known to provide accurate band gaps and molecular dynamics simulations to investigate thermal stability. Our results demonstrate that these monolayer crystals are thermodynamically stable and, depending on the crystal configuration, may exhibit an optically active band gap in the visible frequency range with highly anisotropic effective masses. The former feature is highly desirable for the applicability of these two-dimensional materials in devices compatible with existing silicon-based optoelectronic technology, whereas the latter opens a fundamental exploration avenue toward anisotropic excitonics and hyperbolic plasmon- and/or exciton-polariton physics in these materials and their heterostructures.

II. THEORETICAL FRAMEWORK

A. Explored Si/Ge adamantane structures

The unit cell of Si (or equivalently, Ge) bulk crystals is sketched in Fig. 1(a). From this unit cell, by choosing planes in different crystallographic directions, one can construct planar crystals in a variety of structures, including the gapless materials known as silicene and germanene, see Ref. [13] for an overview. Here, we focus on the structures presented in Fig. 1(b), labeled PADA-I (Si_8H_8 as DSi-I and Ge_8H_8 as DGe-I) and PADA-II (Si_6H_4 as DSi-II and Ge_6H_4 as DGe-II), which bear resemblance with the crystals known as adamantane and diamantane, respectively. Atomic positions of these monolayer crystal structures are provided in the Supplemental Material [23].

In-plane strain is defined as

$$\epsilon = \frac{a - a_0}{a_0}, \quad (1)$$

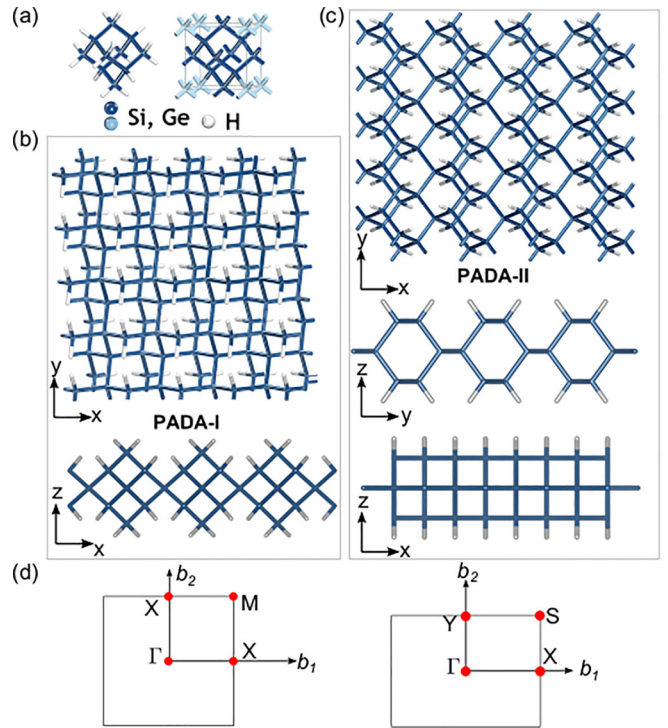


FIG. 1. (a) Sketch of the unit cell of Si- and Ge-based planar adamantane (PADA) crystals, with hydrogen atoms in white (left) and the adjacent atoms in the crystal shown in light blue (right). Two types of planar adamantane crystals can be formed out of this unit cell, labeled here (b) PADA-I and (c) PADA-II, with top and side views. For PADA-I, x and y directions are similar. (d) 2D Brillouin Zone of PADA-I and PADA-II along with high symmetry points.

where a_0 and a denote lattice constants before and after applying in-plane strain. $\epsilon > 0$ corresponds to tensile strain and $\epsilon < 0$ compressive strain.

The formation energy of these compounds on a per atom basis is calculated as

$$E_f = (E - x E_{Si(Ge)} - y E_{H_2}) / (x + y), \quad (2)$$

where E is the energy of system of interest, $E_{Si(Ge)}$ and E_{H_2} are the per atom energies of bulk Si (or Ge, depending upon the material being investigated) and of the isolated H_2 molecule, respectively. x and y denote the number of Si (Ge) and H atoms in the structure. As the free standing monolayers possess higher energy than their bulk counterparts, they all lie above the bulk phases in the formation energy hull. Therefore, we also calculate formation energy with respect to 2D phases of Silicon and Germanium as

$$E_f^{2D} = (E - x E_{Si(Ge),2D} - y E_{H_2}) / (x + y), \quad (3)$$

where symbols have the same meaning as in Eq. (2), but taking monolayer Silicene (Germanene) as reference for Si (Ge) energies.

B. Electronic properties

The calculations were performed using first-principles density functional theory (DFT) as implemented in the

Vienna *ab initio* simulation package (VASP) [24,25]. Projector augmented wave (PAW) [25,26] pseudopotentials were used for the electron-ion interactions. The exchange correlation part of the total energy was approximated by the generalized gradient approximation (GGA) using Perdew-Burke-Ernzerhof (PBE) type of functional [27]. A vacuum of 15 Å is included along the z axis to avoid spurious interactions between the periodic images. To obtain the ground state energy structure a complete structural relaxation was performed using the conjugate-gradient method until the forces were converged to within 0.005 eV/Å. The Brillouin zone was sampled with a well-converged gamma-centered k mesh of $17 \times 17 \times 1$ for PADA-I, and $15 \times 11 \times 1$ for PADA-II compounds. Four valence electrons for Si and Ge (s^2p^2) and one for H were used in the pseudopotential. A plane wave energy cutoff of 550 eV was used for the structural relaxation and electronic structure calculations.

PBE often underestimates the bandgaps, therefore, the electronic properties were reevaluated using the HSE functional [28]. In the HSE calculation, one-fourth of the PBE exchange was replaced by the Hartree-Fock exact exchange ($\alpha = 0.25$), and screening parameter $\mu = 0.20$ was used. This choice of parameters is often termed as the HSE06 functional. Electronic band structure plots and carrier effective masses are computed using the Sumo package [29]. To investigate the possibility of light emission/absorption from the conduction and valence band-edge states of the adamantane monolayers, we calculate the transition dipole moment (TDM) in order to check if transitions between these states are parity forbidden [30]. TDM is defined as the electric dipole moment associated with a transition between the initial state and the final state [30]. The TDM of two energy eigenstates ψ_i and ψ_f with energy E_i and E_f can be written as

$$P_{i \rightarrow f} = \frac{i\hbar}{(E_i - E_f)m} \langle \psi_i | \mathbf{P} | \psi_f \rangle, \quad (4)$$

where m is the free electron mass, and \mathbf{P} is the momentum operator. The transition probability between two eigenstates is defined as a sum of the square moduli of TDM (P^2), as implemented in the VASPKIT [31].

C. Phonon dispersion, mechanical properties, and thermal stability

For phonon dispersion calculations, the atoms in the crystal were displaced by 0.02 Å using the finite displacement supercell approach as implemented within the PHONOPY [32,33] package, and forces for these configurations were calculated using VASP [24,25]. In order to obtain well converged phonon frequencies, a supercell of $4 \times 4 \times 1$ (for PADA-I) and $6 \times 4 \times 1$ (for PADA-II) was used, along with an energy cutoff of 500 eV, and a strict energy convergence criterion of 10^{-8} eV. For all the phonon calculation, Brillouin zone was sampled at a Γ -centered $3 \times 3 \times 1$ k mesh. Translation and rotational invariance together with Born-Huang symmetry constraints were applied on the calculated harmonic interatomic force constants [34,35]. The relaxed- and clamped-ion elastic stiffness tensors are calculated within the small displacement method using stress-strain relationship [36], as implemented in VASP. In addition, the piezoelectric stress coefficients were

directly obtained using density functional perturbation theory (DFPT) [37] with a large k -point grid $27 \times 27 \times 1$ and energy cutoff of 600 eV.

To probe the thermal stability of PADA-I and PADA-II monolayers, *ab initio* molecular dynamics simulations (AIMD) were carried out at 300 K and 600 K, with total simulation time 10 ps in an NVT ensemble. Here, a timestep of 2 fs was used, AIMD simulation was allowed to run for 5000 steps, and $4 \times 4 \times 1$ (256 atoms) and $6 \times 4 \times 1$ (240 atoms) were used for PADA-I and PADA-II compounds, respectively. Temperature was controlled using a Nosé-Hoover thermostat [38] and Γ -point-only was used for Brillouin zone integration.

III. RESULTS AND DISCUSSION

A. Structural, dynamical, mechanical, and thermal stability

First, in order to discuss the energetic feasibility of these compounds, we have calculated their bulk and 2D formation energies as per described in Eqs. (2) and (3), which are included in Table I. When the formation energy is calculated with respect to bulk Si and Ge phases, all four monolayers lie marginally above the convex hull, although energy difference is only <55 meV/atom for Si and <133 meV/atom for Ge monolayers. These small formation energies with respect to bulk phases indicate the possible energetic feasibility of these monolayers. As alluded before, 2D monolayers are often in higher energy than their bulk counterparts, therefore, we also calculate the formation energy with respect to 2D phases of Si and Ge (E_f^{2D}), namely Silicene and Germanene, respectively. As verified in Table I, the E_f^{2D} of these monolayers is negative. For comparison, we also calculated the E_f^{2D} formation energies of these structures without hydrogen, which are much higher than the corresponding hydrogenated monolayer. This indicates the hydrogenation is an energetically favorable process to realize the monolayer of Si and Ge. Next, we address the dynamical stability of Si and Ge adamantane and diamantane 2D crystals, by calculating the phonon dispersions as shown in Fig. 2. The dynamical stability of the DSi-I, DGe-I, DSi-II, and DGe-II monolayers is validated since phonon dispersions for neither of the four investigated structures exhibited imaginary phonon frequencies. Next the mechanical properties of these structures are examined by calculating the elastic-stiffness tensor components, which are listed in Table I. We find that all four considered structures are mechanically stable and obey the Born stability criteria. For example, the tetragonal symmetry structure (PADA-I) should satisfy $C_{11} > 0$, $C_{33} > 0$, and $C_{11} > C_{12}$. Similarly, for the orthorhombic structure (PADA-II), $C_{11} > 0$, $C_{33} > 0$, and $C_{11}C_{22} > C_{12}^2$ should be satisfied. As one verifies in Table I, all necessary and sufficient conditions for elastic stability are indeed fulfilled.

It has been shown that hydrogen atoms may diffuse both in bulk silicon and at its surface [39–43], therefore it is necessary to check the stability of these monolayers at finite temperatures. In order to probe the thermal stability of these structures we also performed AIMD simulations using an NVT ensemble with constant particle number, volume, and temperature. These results are shown in Figs. 3(a) and 3(b) for DSi-I and

TABLE I. Calculated bulk (E_f) and 2D (E_f^{2D}) formation energies, elastic and piezoelectric coefficient for DSi-I, DGe-I, DSi-II, and DGe-II crystals. Due to crystal symmetry in DSi-I and DGe-I, $C_{11} = C_{22}$. DSi-II and DGe-II belong to a centrosymmetric space group and therefore do not exhibit piezoelectricity. Values in the parenthesis correspond to E_f^{2D} formation energy of these phases without H atoms. After removing hydrogen the PADA-II phases relax in the dumbbell structure.

System	E_f	E_f^{2D}	Elastic tensor (N/m)				e_{ij} (pC/m)		d_{ij} (pm/V)	
	(eV/atom)	(eV/atom)	C_{11}	C_{22}	C_{12}	C_{33}	e_{14}	e_{36}	d_{14}	d_{36}
DGe-I	0.132	−0.107 (0.10)	34.88	34.88	21.14	26.68	33.70	6.80	1.52	0.26
DSi-I	0.055	−0.265 (0.14)	42.31	42.31	27.55	31.95	28.40	3.10	1.16	0.10
DGe-II	0.105	−0.182 (−0.06)	81.14	27.17	8.85	22.88				
DSi-II	0.33	−0.350 (−0.097)	100.36	34.83	11.34	27.32				

DSi-II. The simulation snapshots are also shown at the 4 and 8 ps. Although the computed potential energy slightly fluctuates along the simulation time, no considerable lowering of potential energy over time is observed. Within the simulation duration and temperature range explored here, hydrogen atoms are always bonded with Si atoms and no hydrogen diffusion in the lattice is observed. Moreover, as one verifies in the presented snapshots, apart from minor distortions, the crystallinity of DSi-I and DSi-II structures is preserved even at a temperature as high as 600 K. Similar results for DGe-I and DGe-II are included in the Supplemental Material [23]. AIMD simulations are computationally very expensive, therefore we have limited our investigations up to 600 K. Although these results do not fully guarantee the thermal stability of these monolayers (as the results of AIMD simulation tend to vary with respect to super-cells size, simulations duration, and temperature), they surely indicate the possibility of these structures being stable at high temperatures.

B. Piezoelectricity

The piezoelectric effect is known to generate an electric dipole moment as a result of applied mechanical stress in noncentrosymmetric materials. Theoretical predictions and experimental observations [44–47] have demonstrated that in 2D materials the piezoelectric constants can be enhanced. Among the materials studied here, PADA-I crystals are noncentrosymmetric and are expected to exhibit piezoelectricity, whereas PADA-II crystals are centrosymmetric and, thus, do not show piezoelectric properties. The application of strain induces polarization in noncentrosymmetric crystals, which is described by the third-rank piezoelectric stress e_{ij} , and the strain tensor d_{ij} . e_{ij} is related to d_{ik} by elastic stiffness tensor elements C_{ik} as per

$$e_{ij} = d_{ik}C_{ik}. \quad (5)$$

The PADA-I monolayers have $P\bar{4}2_1m$ symmetry (space group 111 and point group $\bar{4}2m$). Considering the crystal symmetry, the tensor equation (5) can be rewritten as

$$\begin{pmatrix} e_{14} & 0 & 0 \\ 0 & e_{14} & 0 \\ 0 & 0 & e_{36} \end{pmatrix} = \begin{pmatrix} d_{14} & 0 & 0 \\ 0 & d_{14} & 0 \\ 0 & 0 & d_{36} \end{pmatrix} \begin{pmatrix} C_{11} & C_{12} & 0 \\ C_{12} & C_{22} & 0 \\ 0 & 0 & C_{66} \end{pmatrix}. \quad (6)$$

Solving Eq. (6) for the nonzero tensor elements yields

$$d_{14} = e_{14} \frac{C_{11}}{C_{11}^2 - C_{12}^2}; \quad d_{36} = \frac{e_{36}}{C_{66}}. \quad (7)$$

Here, d_{14} and d_{36} stand for induced polarization in the x or z direction when the strain is applied in the yz or xy direction, respectively. The computed relaxed-ion piezoelectric constants are listed in Table I. The calculated relaxed ion piezoelectric coefficients for both DSi-I ($d_{14} = 1.16$ pm/V) and DGe-I ($d_{14} = 1.52$ pm/V) crystals are smaller than the coefficients for MoS₂ and larger than those for h-BN [44]. Previous reports have shown that under functionalization with hydrogen and/or fluorine, the piezoelectric properties of silicene can be significantly improved [48]. It was shown that hydrogen and fluorine codecorated silicene exhibit d_{31} value of 1.6 pm/V, which is comparable to our calculated values for PADA-I monolayers. Therefore, we conclude that adamantane silicon and germanium monolayers are promising for further flexo- and piezoelectric studies and purposes.

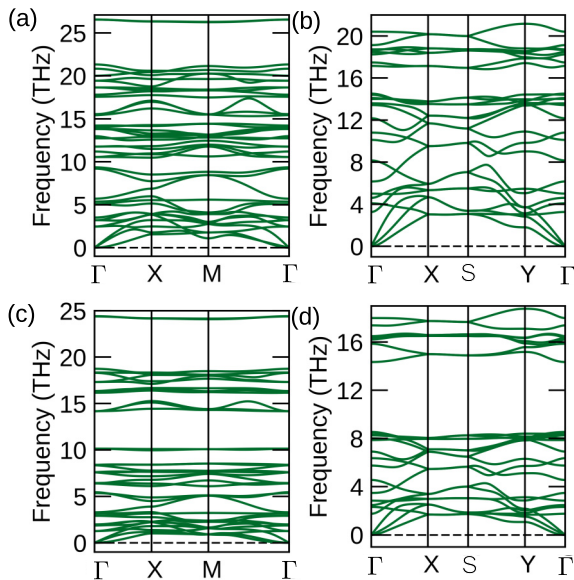


FIG. 2. Phonon dispersions of Si and Ge PADA-I [panels (a) and (c), respectively] and PADA-II monolayers [panels (b) and (d), respectively]. For better visualization, only the low frequency portion of phonon dispersion is shown. The hydrogen phonon modes here extend up to ~ 64 THz.

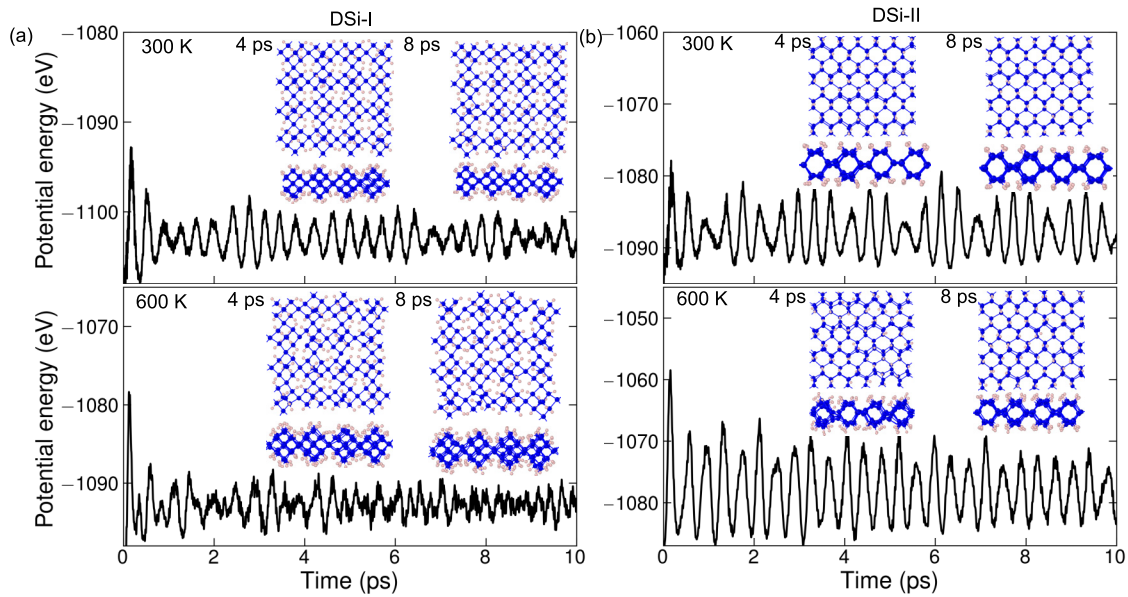


FIG. 3. Potential energy profiles for (a) DSi-I and (b) DSi-II structures during the AIMD simulations at 300 K (top panel) and 600 K (bottom panel), respectively. The snapshots of corresponding atomic configurations are also shown at 4 ps and 8 ps.

C. Electronic structure

The band structures of Si and Ge adamantane and diamantane monolayers, as obtained with HSE06 functional, are shown in Fig. 4 and Eq. (5). While the DGe-II (DSi-II) monolayer exhibits an indirect (direct) gap in the infrared range, both DGe-I and DSi-I monolayers exhibit *direct* band gaps in the blue-violet range, which is of significance toward optoelectronic applications. Notice that the actual optical gap is still expected to be redshifted by a few hundred meV due to exciton binding energy.

It is possible that light-induced transitions between the conduction and valence band edge states in the direct gap structures, found here for PADA-I monolayers as well as DSi-II, are in fact forbidden by symmetry rules. The latter

would obviously hinder the application of these materials in optoelectronics. To check, we therefore calculate the transition dipole moment (TDM) between band-edge states using Eq. (4) at each point of the first Brillouin zone. Results are shown in the bottom panels of Figs. 4 and 5, where we observe that the dipole moment at the gap (Γ point) is significant only for the DSi-I and DGe-II. This allows us to conclude that Si and Ge PADA-I monolayers are stable and exhibit optically active direct gap near blue-violet range.

From the top panels of Figs. 4 and 5, one clearly observes that Si and Ge in both PADA-I and PADA-II monolayer crystal forms exhibit highly anisotropic band structures both for electrons and holes, where holes in the former exhibit particularly high effective masses (i.e., almost flat bands) in the Γ M direction. Electron and hole effective masses, as

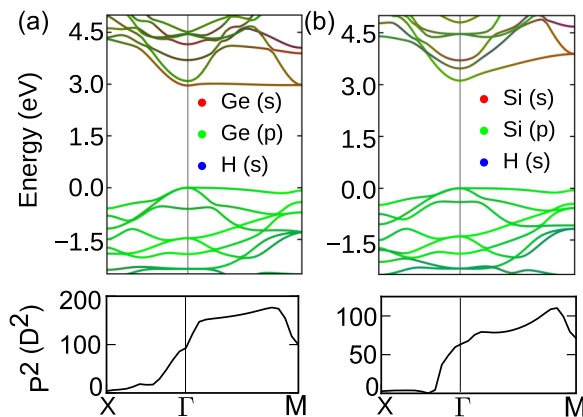


FIG. 4. Calculated band structures (top panel) and transition dipole moments (in units of Debye, bottom panel) of (a) Ge and (b) Si monolayers with PADA-I crystal configuration, as obtained with HSE functionals. The top of the valence band is taken as the energy reference. The colors represent the orbital contributions in each state.

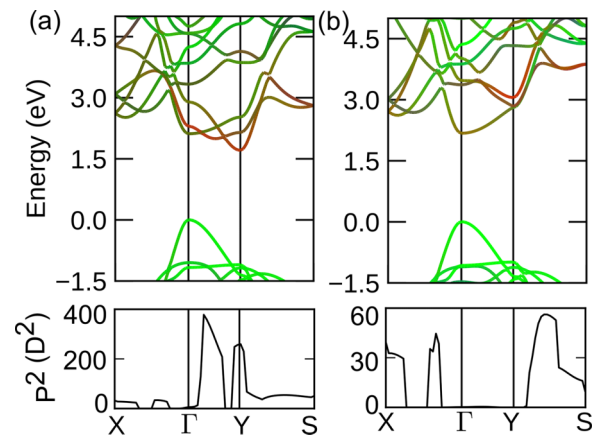


FIG. 5. Calculated band structures (top panel) and transition dipole moments (bottom panel) of (a) Ge and (b) Si monolayers with PADA-II crystal configuration, as obtained with HSE functionals. The top of the valence band is taken as the energy reference. The color code is the same as in Fig. 4.

TABLE II. HSE06 calculated bandgaps in (eV) and carrier effective masses (in units of the free electron mass m_0) along different directions in PADA-I and PADA-II Si and Ge monolayers. In PADA-I monolayers, effective masses are calculated along ΓX and ΓM directions, whereas in PADA-II monolayers, they are calculated along ΓX and ΓY directions. The PBE bandgaps and effective masses are given in parenthesis.

System	Bandgap (eV)	Effective mass (m)			
		hole		electron	
		Γ -X	Γ -M (I) Γ -Y (II)	Γ -X	Γ -M (I) Γ -Y (II)
DGe-I	2.96 (2.17)	0.36 (0.33)	12.10 (11.89)	0.24 (0.23)	11.7 (11.5)
DSi-I	3.11 (2.33)	0.50 (0.51)	13.52 (12.48)	0.22 (0.22)	0.29 (0.24)
DGe-II	1.70 (1.04)	0.09 (0.08)	0.47 (0.49)	0.14 (0.11)	0.10 (0.28)
DSi-II	2.17 (1.50)	0.15 (0.15)	0.54 (0.56)	0.12 (0.12)	1.52 (1.67)

calculated from the band curvatures at Γ , are presented in Table II. The effective masses have also been calculated using both PBE (values within parenthesis in Table II). The PBE values of the effective masses are in good agreement in terms of the order of magnitude with the HSE06 ones. Notably, the hole effective masses both in Si and Ge PADA-I structures reach tens of the free-electron mass m in the ΓM direction, while being nearly two orders of magnitude lower in the ΓX direction. Electron bands are also significantly anisotropic in all structures, except for the DSi-I case. Such high anisotropy of electron and hole bands in PADA-I and PADA-II

monolayers is expected to motivate future studies involving, e.g., transport properties with anisotropic mobilities [49,50], as well as optoelectronic properties with hyperbolic plasmon or excitonpolaritons, in a similar fashion as discussed in other anisotropic 2D materials such as black phosphorus and transition metal trichalcogenides [51–56].

D. Strain effects on the band gap and effective masses

As is characteristic for 2D materials, the electronic band structures of the Si and Ge monolayers investigated here are prone to tunability via mechanical stress. Before exploring their strain dependent electronic properties, let us first investigate the dynamical stability of these strained systems by performing phonon calculations under various compressive and tensile strains. Figures 6 and 7 show the calculated phonon dispersions for strained PADA-I and PADA-II compounds, respectively. Figure 6 shows that PADA-I monolayers become dynamically unstable (i.e., they exhibit negative phonon frequencies) even for compressive strains as small as 2%, whereas the DGe-II (DSi-II) monolayer in Fig. 7 remains dynamically stable for compressive strains up to 10% (8%). As for tensile strain, both PADA-I and PADA-II systems remain dynamically stable at least up to +20%. Therefore, in what follows, the strain dependent electronic properties of PADA-I monolayers will be investigated here only under tensile strain, where they are clearly stable, while electronic properties of PADA-II systems will be discussed under both compressive and tensile strain.

Figure 8(a) shows the calculated energy gap of all the Si and Ge PADA-I and PADA-II monolayers as a function of applied biaxial compressive (negative) and tensile (positive) strain. Details of their band structures are shown in Figs. S1 and S2 in the Supplemental Material [23]. The gaps in all

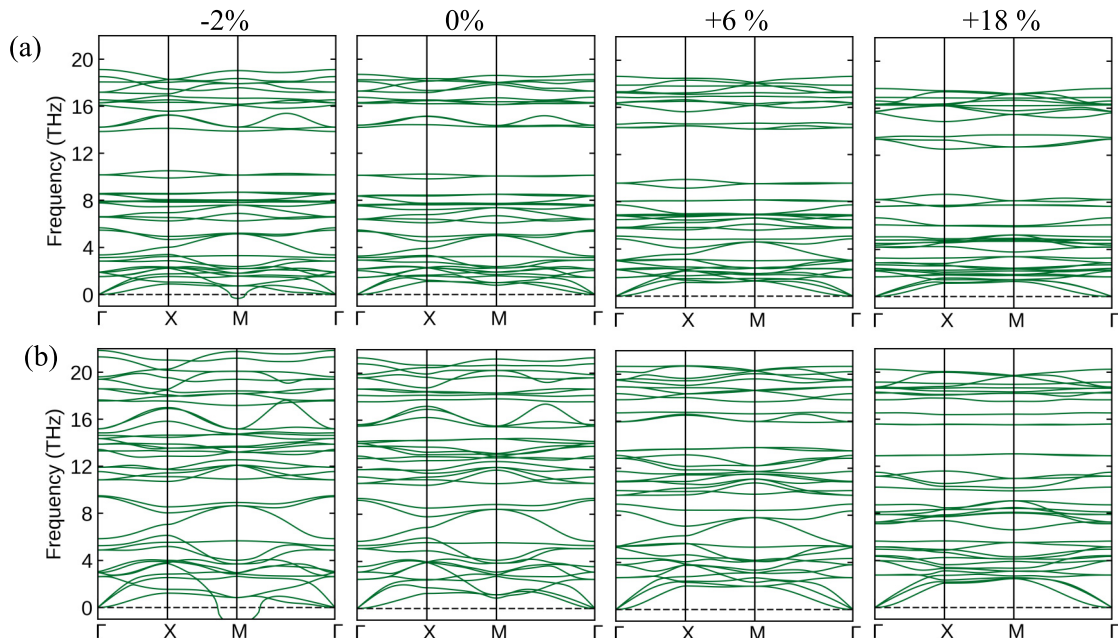


FIG. 6. Phonon dispersion of (a) DGe-I and (b) DSi-I under selected compressive (–) and tensile strains (+). Both compounds remain dynamically stable up to 18% tensile strain, whereas they both become unstable at 2% compressive strain.

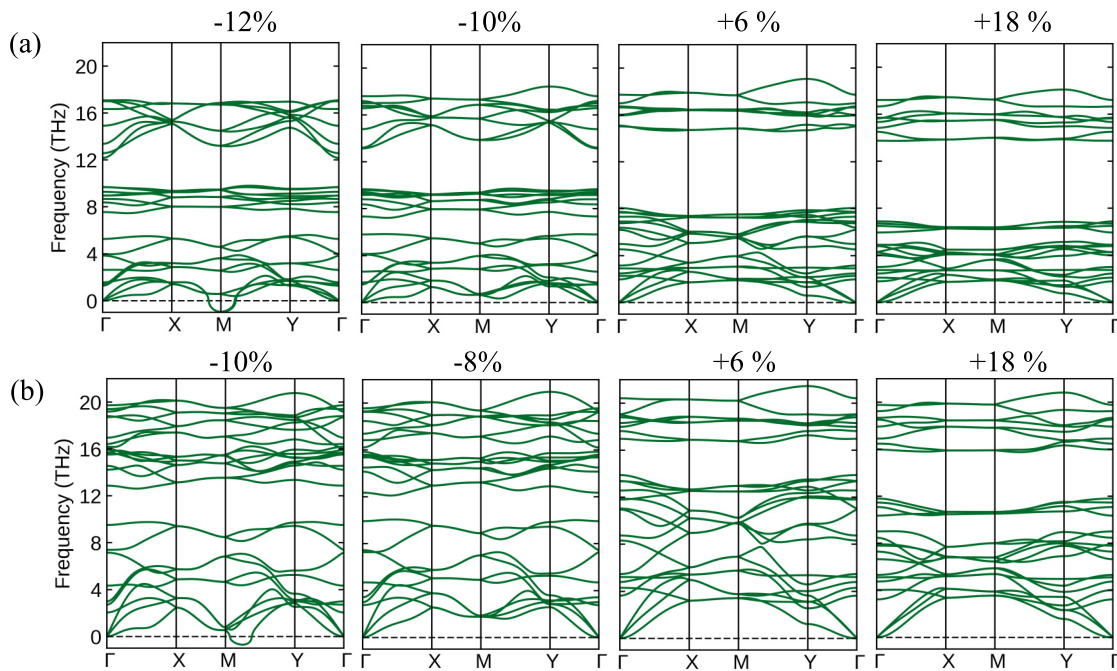


FIG. 7. Phonon dispersion of (a) DGe-II and (b) DSi-II under selected compressive (−) and tensile strains (+). Both compounds remain dynamically stable up to 18% tensile strain, whereas DGe-II (DSi-II) becomes unstable at 12% (10%) compressive strain.

cases are significantly reduced by strain and, particularly, DGe-II becomes metallic at threshold tensile strain value of 14%. Interestingly, strain enables transitions from indirect to direct characters of the gap in several cases. The gaps of PADA-I Ge and Si monolayers, which are both direct in the absence of strain (see Fig. 4), become indirect at high values of tensile strain. Conversely, DGe-II exhibits an indirect gap in the absence of strain (see Fig. 5), which becomes direct at 6% tensile (8% compressive) strain. As for DSi-II, it exhibits a direct gap without strain, which remains direct for all values of strain investigated here. Under compressive strain, the bandgap of DSi-II becomes indirect as the strain exceeds 4%, but becomes direct again for strain larger than 7%. Even so, in all the observed transitions from indirect to direct gap in PADA-II monolayers, we have verified that the dipole moment for their conduction and valence states around the gap remains zero, just as observed for the unstrained case in Fig. 5. Therefore, despite the observed strain-induced direct gap character, the PADA-II monolayers remain less relevant for optoelectronics applications as compared to the Si and Ge PADA-I systems.

In order to understand the effect of applied tensile strain on the band curvatures, we plot in Figs. 8(b)–8(e) the carrier effective masses along selected high symmetric directions for both hole (negative values) and electron (positive values). As observed in Figs. 8(b) and 8(c), tensile strain significantly reduces the hole effective masses along ΓM direction in both PADA-I compounds. For instance, at zero strain, holes in DGe-I have an effective mass $12.5m_0$ along ΓM which, at 18% tensile strain, becomes $2.1m_0$. Similarly, the hole effective mass along the same direction in DSi-I reduces from $13.2m_0$, at zero strain, to $1.5m_0$ at 18% tensile strain. The high electron effective mass along ΓM in DGe-I is also strongly sensitive

to the applied tensile strain and can be significantly tuned, see Fig. 8(b), whereas for DSi-I those masses are much less sensitive to strain. Effective masses for electrons in PADA-I crystals along the ΓX direction are not significantly modified by strain and, therefore, are not shown in the Figs. 8(b) and 8(c). As for the PADA-II compounds, in both Si and Ge variants, the hole effective mass monotonically decreases with tensile strain, see Figs. 8(d) and 8(e), although with much weaker dependence as compared to the PADA-I cases. Similarly, the electron effective masses also decrease with tensile strain. The crossover in electron effective masses in DGe-II around 6% tensile strain is associated with the previously discussed indirect-to-direct bandgap transition.

The control of carrier effective masses via strain, as demonstrated here, allows one to tune carrier mobilities in the Si and Ge adamantane/diamantane monolayers. Within the deformation potential theory, mobility of charge carriers in a material is inversely proportional to the square of their effective masses [50,57]; hence, the observed drastic reduction in carrier effective masses, particularly in PADA-I compounds, is expected to lead to significant enhancement in carrier mobilities of these monolayer crystals.

IV. CONCLUSIONS

In summary, we have presented first-principles calculations of the electronic, vibrational, and mechanical properties of the diamondoidlike Si and Ge monolayers. Both their adamantane and diamantane structures, labeled here PADA-I and PADA-II, respectively, are found thermodynamically, dynamically, and mechanically stable.

Si and Ge diamantane (PADA-II) monolayers are both semiconductors, with gaps of ≈ 2.17 eV and ≈ 1.7 eV,

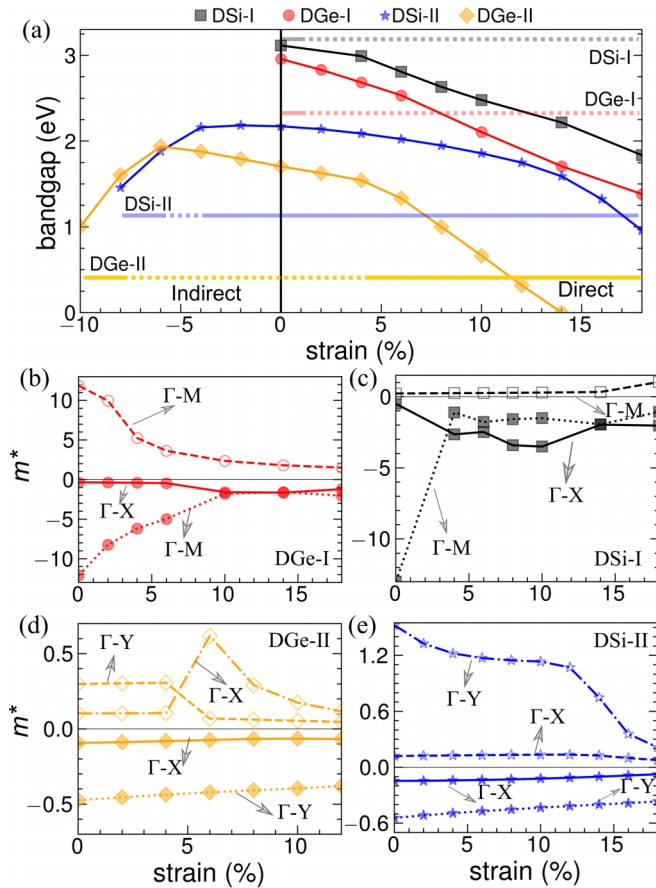


FIG. 8. (a) Dependence of the band gaps of PADA-I Si (DSi-I) and Ge (DGe-I), and PADA-II Si (DSi-II) and Ge (DGe-II) monolayers on applied biaxial strain. Negative (−) and positive (+) strain values correspond to compressive and tensile strains, respectively. The vertical solid line at 0% is a guide to the eyes. Horizontal solid and dotted lines indicate the strain region where the bandgap is direct and indirect, respectively. Variation of carrier effective masses m^* (in units of the free electron mass m_0) under tensile strain is shown for DGe-I (b), DSi-I (c), DGe-II (d), and DSi-II (e).

respectively, and qualitatively similar valence bands. However, they exhibit strikingly different conduction bands—while the DSi-II has a direct gap, with the conduction band minimum at the Γ point, the DGe-II exhibits indirect gap, with conduction band minimum at the Y point. Nevertheless, the direct gap in DSi-II is not optically active, as verified by the zero dipole moment between conduction and valence bands at the Γ point. On the other hand, calculations of the strain tensor components of the PADA-II Si and Ge crystals reveal that they are both very good piezoelectric materials.

Differently from PADA-II structures, the DSi-I and DGe-I both exhibit optically active direct gaps of ≈ 3.11 eV and ≈ 2.96 eV, respectively, with highly anisotropic effective masses. We showed that these gaps and effective masses can be broadly tuned via applied strain. The relevance of this result is twofold: (i) the optically active gap in DSi-I and DGe-I enables their use in optoelectronic devices with a frequency range from near the blueviolet down to the red (under strain) which would be naturally compatible and easily integrated with current silicon-based technologies, and (ii) the strong effective mass anisotropy observed here renders these materials and their heterostructures a platform for the investigation of anisotropic, possibly hyperbolic, polaritons, as well as the emergent anisotropic excitonic phenomena and correlated phases.

ACKNOWLEDGMENTS

This work was financially supported through the PQ and UNIVERSAL programs of the Brazilian Council for Research (CNPq), and by the Research Foundation - Flanders (FWO). T.P. is supported by the FWO postdoctoral fellowship. The computational resources and services used in this work were provided by the VSC (Flemish Supercomputer Center), and funded by the FWO and the Flemish Government department EWI.

- [1] K. D. Sattler, *Silicon Nanomaterials Sourcebook: Low-Dimensional Structures, Quantum Dots, and Nanowires* (CRC Press, Boca Raton, FL, 2017), Vol. 1.
- [2] Y. Guo, Q. Wang, Y. Kawazoe, and P. Jena, A new silicon phase with direct band gap and novel optoelectronic properties, *Sci. Rep.* **5**, 14342 (2015).
- [3] D. R. Lide, *CRC Handbook of Chemistry and Physics* (CRC press, Boca Raton, FL, 2004), Vol. 85.
- [4] H. Itahara and H. Nakano, Synthesis and optical properties of two-dimensional nanosilicon compounds, *Jpn. J. Appl. Phys.* **56**, 05DA02 (2017).
- [5] M. Bruno, M. Palummo, S. Ossicini, and R. Del Sole, First-principles optical properties of silicon and germanium nanowires, *Surf. Sci.* **601**, 2707 (2007).
- [6] M.-F. Ng, M. B. Sullivan, S. W. Tong, and P. Wu, First-principles study of silicon nanowire approaching the bulk limit, *Nano Lett.* **11**, 4794 (2011).
- [7] Z. L. Wang, *Nanowires and Nanobelts: Materials, Properties and Devices. Volume 1: Metal and Semiconductor Nanowires* (Springer Science & Business Media, 2013).
- [8] J. D. Cressler and G. Niu, *Silicon-Germanium Heterojunction Bipolar Transistors* (Artech house, 2003).
- [9] A. Chroneos and H. Bracht, Diffusion of n-type dopants in germanium, *Appl. Phys. Rev.* **1**, 011301 (2014).
- [10] C. Boztug, J. R. Sánchez-Pérez, F. Cavallo, M. G. Lagally, and R. Paiella, Strained-germanium nanostructures for infrared photonics, *ACS Nano* **8**, 3136 (2014).
- [11] L. Tao, E. Cinquanta, D. Chiappe, C. Grazianetti, M. Fanciulli, M. Dubey, A. Molle, and D. Akinwande, Silicene field-effect transistors operating at room temperature, *Nat. Nanotechnol.* **10**, 227 (2015).
- [12] A. Molle, C. Grazianetti, L. Tao, D. Taneja, M. H. Alam, and D. Akinwande, Silicene, silicene derivatives, and their device applications, *Chem. Soc. Rev.* **47**, 6370 (2018).

- [13] P. Borlido, C. Rödl, M. A. Marques, and S. Botti, The ground state of two-dimensional silicon, *2D Mater.* **5**, 035010 (2018).
- [14] Y. Ding and Y. Wang, Tunable electronic structures of hydrogenated zigzag and armchair dumbbell silicene nanosheets: A computational study, *J. Phys. Chem. C* **122**, 23208 (2018).
- [15] Y. F. Li, G. H. Tang, and B. Fu, Hydrogenation: An effective strategy to improve the thermoelectric properties of multilayer silicene, *Phys. Rev. B* **99**, 235428 (2019).
- [16] T. Leoni, C. Hogan, K. Zhang, M. Daher Mansour, R. Bernard, R. Parret, A. Resta, S. Colonna, Y. Borensztein, F. Ronci *et al.*, Demonstration of the existence of dumbbell silicene: A stable two-dimensional allotrope of silicon, *J. Phys. Chem. C* **125**, 17906 (2021).
- [17] J. Qiu, H. Fu, Y. Xu, Q. Zhou, S. Meng, H. Li, L. Chen, and K. Wu, From silicene to half-silicene by hydrogenation, *ACS Nano* **9**, 11192 (2015).
- [18] Q. Yao, L. Zhang, N. Kabanov, A. Rudenko, T. Arjmand, H. Rahimpour Soleimani, A. Klavsyuk, and H. Zandvliet, Bandgap opening in hydrogenated germanene, *Appl. Phys. Lett.* **112**, 171607 (2018).
- [19] J. Dahl, S. Liu, and R. Carlson, Isolation and structure of higher diamondoids, nanometer-sized diamond molecules, *Science* **299**, 96 (2003).
- [20] W. A. Clay, J. Dahl, R. Carlson, N. Melosh, and Z. Shen, Physical properties of materials derived from diamondoid molecules, *Rep. Prog. Phys.* **78**, 016501 (2015).
- [21] A. Santos, E. Moreira, A. Meiyazhagan, and D. Azevedo, Bond order effects on the optoelectronic properties of oxygen/sulfur functionalized adamantanes, *J. Mol. Graphics Modell.* **105**, 107869 (2021).
- [22] F. Marsusi, K. Mirabbaszadeh, and G. Ali Mansoori, Optoelectronic properties of adamantane and hydrogen-terminated sila- and germa-adamantane: A comparative study, *Physica E* **41**, 1151 (2009).
- [23] See Supplemental Material at <http://link.aps.org/supplemental/10.1103/PhysRevB.108.035302> for AIMD simulations of DGe-I and DGe-II, information on atomic positions in the crystal structures and electronic band structures of Si and Ge adamantane and diamantane monolayers under strain.
- [24] G. Kresse and J. Furthmüller, Efficiency of *ab-initio* total energy calculations for metals and semiconductors using a plane-wave basis set, *Comput. Mater. Sci.* **6**, 15 (1996).
- [25] G. Kresse and D. Joubert, From ultrasoft pseudopotentials to the projector augmented-wave method, *Phys. Rev. B* **59**, 1758 (1999).
- [26] P. E. Blöchl, Projector augmented-wave method, *Phys. Rev. B* **50**, 17953 (1994).
- [27] J. P. Perdew, K. Burke, and M. Ernzerhof, Generalized Gradient Approximation Made Simple, *Phys. Rev. Lett.* **77**, 3865 (1996).
- [28] J. Heyd, J. E. Peralta, G. E. Scuseria, and R. L. Martin, Energy band gaps and lattice parameters evaluated with the Heyd-Scuseria-Ernzerhof screened hybrid functional, *J. Chem. Phys.* **123**, 174101 (2005).
- [29] A. M. Ganose, A. J. Jackson, and D. O. Scanlon, Sumo: Command-line tools for plotting and analysis of periodic *ab initio* calculations, *J. Open Source Softw.* **3**, 717 (2018).
- [30] W. Meng, X. Wang, Z. Xiao, J. Wang, D. B. Mitzi, and Y. Yan, Parity-forbidden transitions and their impact on the optical absorption properties of lead-free metal halide perovskites and double perovskites, *J. Phys. Chem. Lett.* **8**, 2999 (2017).
- [31] V. Wang, N. Xu, J.-C. Liu, G. Tang, and W.-T. Geng, VASPKIT: A user-friendly interface facilitating high-throughput computing and analysis using VASP code, *Comput. Phys. Commun.* **267**, 108033 (2021).
- [32] A. Togo, L. Chaput, and I. Tanaka, Distributions of phonon lifetimes in Brillouin zones, *Phys. Rev. B* **91**, 094306 (2015).
- [33] A. Togo and I. Tanaka, First principles phonon calculations in materials science, *Scr. Mater.* **108**, 1 (2015).
- [34] M. Born and K. Huang, *Dynamical Theory of Crystal Lattices* (Clarendon press, 1954).
- [35] C. A. Polanco, T. Pandey, T. Berlijn, and L. Lindsay, Defect-limited thermal conductivity in MoS₂, *Phys. Rev. Mater.* **4**, 014004 (2020).
- [36] Y. Le Page and P. Saxe, Symmetry-general least-squares extraction of elastic data for strained materials from *ab initio* calculations of stress, *Phys. Rev. B* **65**, 104104 (2002).
- [37] X. Wu, D. Vanderbilt, and D. R. Hamann, Systematic treatment of displacements, strains, and electric fields in density-functional perturbation theory, *Phys. Rev. B* **72**, 035105 (2005).
- [38] S. Nosé, A molecular dynamics method for simulations in the canonical ensemble, *Mol. Phys.* **52**, 255 (1984).
- [39] C. G. Van de Walle, Hydrogen in silicon: Fundamental properties and consequences for devices, *J. Vac. Sci. Tech. A: Vac. Surf. Films* **16**, 1767 (1998).
- [40] B. Sopori, X. Deng, J. Benner, A. Rohatgi, P. Sana, S. Estreicher, Y. Park, and M. Roberson, Hydrogen in silicon: A discussion of diffusion and passivation mechanisms, *Sol. Energy Mater. Sol. Cells* **41-42**, 159 (1996).
- [41] M. Dürr and U. Höfer, Hydrogen diffusion on silicon surfaces, *Prog. Surf. Sci.* **88**, 61 (2013).
- [42] H. Xu, Electronic structure of hydrogen-vacancy complexes in crystalline silicon: A theoretical study, *Phys. Rev. B* **46**, 1403 (1992).
- [43] M. A. Roberson and S. K. Estreicher, Vacancy and vacancy-hydrogen complexes in silicon, *Phys. Rev. B* **49**, 17040 (1994).
- [44] K.-A. N. Duerloo, M. T. Ong, and E. J. Reed, Intrinsic piezoelectricity in two-dimensional materials, *J. Phys. Chem. Lett.* **3**, 2871 (2012).
- [45] T. Wu and H. Zhang, Piezoelectricity in two-dimensional materials, *Angew. Chem., Int. Ed.* **54**, 4432 (2015).
- [46] M. N. Blonsky, H. L. Zhuang, A. K. Singh, and R. G. Hennig, *Ab initio* prediction of piezoelectricity in two-dimensional materials, *ACS Nano* **9**, 9885 (2015).
- [47] R. Hinchet, U. Khan, C. Falconi, and S.-W. Kim, Piezoelectric properties in two-dimensional materials: Simulations and experiments, *Mater. Today* **21**, 611 (2018).
- [48] M. Noor-A-Alam, H. J. Kim, and Y.-H. Shin, Hydrogen and fluorine co-decorated silicene: A first principles study of piezoelectric properties, *J. Appl. Phys.* **117**, 224304 (2015).
- [49] H. Du, X. Lin, Z. Xu, and D. Chu, Recent developments in black phosphorus transistors, *J. Mater. Chem. C* **3**, 8760 (2015).
- [50] J. Qiao, X. Kong, Z.-X. Hu, F. Yang, and W. Ji, High-mobility transport anisotropy and linear dichroism in few-layer black phosphorus, *Nat. Commun.* **5**, 4475 (2014).
- [51] F. Wang, C. Wang, A. Chaves, C. Song, G. Zhang, S. Huang, Y. Lei, Q. Xing, L. Mu, Y. Xie *et al.*, Prediction of hyperbolic exciton-polaritons in monolayer black phosphorus, *Nat. Commun.* **12**, 5628 (2021).

- [52] E. van Veen, A. Nemilentsau, A. Kumar, R. Roldán, M. I. Katsnelson, T. Low, and S. Yuan, Tuning Two-Dimensional Hyperbolic Plasmons in Black Phosphorus, *Phys. Rev. Appl.* **12**, 014011 (2019).
- [53] J. Zhao, D. Ma, C. Wang, Z. Guo, B. Zhang, J. Li, G. Nie, N. Xie, and H. Zhang, Recent advances in anisotropic two-dimensional materials and device applications, *Nano Res.* **14**, 897 (2021).
- [54] E. Torun, H. Sahin, A. Chaves, L. Wirtz, and F. M. Peeters, *Ab initio* and semiempirical modeling of excitons and trions in monolayer TiS_3 , *Phys. Rev. B* **98**, 075419 (2018).
- [55] A. Khatibi, R. H. Godiksen, S. B. Basuvalingam, D. Pellegrino, A. A. Bol, B. Shokri, and A. G. Curto, Anisotropic infrared light emission from quasi-1D layered TiS_3 , *2D Mater.* **7**, 015022 (2020).
- [56] A. Pant, E. Torun, B. Chen, S. Bhat, X. Fan, K. Wu, D. P. Wright, F. M. Peeters, E. Soignard, H. Sahin *et al.*, Strong dichroic emission in the pseudo one dimensional material ZrS_3 , *Nanoscale* **8**, 16259 (2016).
- [57] A. Manjanath, A. Samanta, T. Pandey, and A. K. Singh, Semiconductor to metal transition in bilayer phosphorene under normal compressive strain, *Nanotechnology* **26**, 075701 (2015).